RSC Advances

ROYAL SOCIETY OF CHEMISTRY

PAPER

View Article Online
View Journal | View Issue

Cite this: *RSC Adv.*, 2026, **16**, 16824

Strain-engineered Si-doped $Cs_3Bi_2I_9$ perovskite for high-performance MIM capacitors: a DFT study

Yahaya Saadu Itas, *[ab] Mayeen Uddin Khandaker*[acd] and Faiza Benabdallah[e]

Received 15th February 2026
Accepted 20th March 2026

DOI: 10.1039/d6ra01339b

rsc.li/rsc-advances

This study examines the energy storage potential of strain engineered Si doped $Cs_3Bi_2I_9$ perovskites using density functional theory. Key electronic and electromechanical parameters—band gap, born effective charge, polarization, piezoelectricity, and leakage suppression—were evaluated for intrinsic and strained systems. Undoped $Cs_3Bi_2I_9$ exhibits a wide 3.3 eV band gap and low polarization, making it suitable as a stable insulating material. Introducing 0.25 mol% Si narrows the band gap and introduces beneficial defects that enhance the dielectric constant and capacitance, with BEC analysis revealing strong local polarization around Si atoms and increased anisotropic stiffness. Under 0.10% strain, the 0.25 mol% Si doped system achieves polarization nearing 1C m^{-2}, strong out of plane piezoelectricity, and reduced leakage—properties ideal for flexible electronics and energy storage devices. In contrast, 0.50 mol% Si under strain shows excessive polarization and higher leakage due to larger lattice distortion. This work provides the first demonstration that Si-doping synergistically combined with strain-engineering can unlock high-κ dielectric behavior and enhanced polarization in $Cs_3Bi_2I_9$, establishing a new, lead-free perovskite platform for next-generation MIM capacitors.

1 Introduction

In the global community, energy conservation and energy harvesting are crucial for many types of power sources.[1] Batteries and capacitors are the commonly known sources of power globally, which provide a solution for the imbalance between limited energy transmission and renewable energy generation.[2] In most cases, batteries and other metal-insulator-metal (MIM) capacitors significantly suffer from problems of low power density and efficiency due to the nature of the constituent materials.[3] Despite this, MIM capacitors are widely adopted for various applications such as mixed integrated circuits (ICs), radio frequency (RF) circuits and sensor application devices.[4] According to the various literature, the most challenging aspect of MIM capacitor technology is the choice of an efficient material to supress leakage with high precision.[5,6] To contain this challenge, it is necessary to produce dielectric materials with a high polarization response under an electric field, otherwise known as field induced polarization switching.[7] Based on high performance and durability, silicon-based materials are the most used dielectrics in MIM capacitors, because they offer high dielectric constant, excellent thermal and chemical stability, low leakage, and doping flexibility.[8,9] Regarding this, several silicon-based oxides have been reported. For example, Soon-Jin fabricated a silicon nitride-based MIM capacitor for InGaP/GaAs HBT applications, achieving a capacitance density of 600 pF mm^{-2} with breakdown electric fields of 3.0–7.3 MV cm^{-1}.[10] Another study conducted by Federico *et al.* revealed that SiO_2 MIM capacitors performed better in amorphous states.[11] According to Mahata *et al.*, the performance of $TaYO_x$ films (deposited on Au/SiO_2) MIM capacitors depends on dielectric thickness and dielectric breakdown voltage.[12]

Despite their performance, normal silicon-based leakage barriers still suffer from polarization and charge distribution problems.[13] They also tend to reduce performance under mechanical stress.[14] Recently, reviews by various researchers have foreseen silicon-based perovskites as future dielectric materials, which can serve as efficient leakage barriers in MIM capacitors.[15,16] This is because of their much higher dielectric constant than conventional silicon-based dielectrics.[17] Unlike conventional silicon-based dielectrics, perovskite-based dielectrics are multifunctional (dielectric + semiconducting + optoelectronic) and highly compatible with emerging technologies. For example, silicon-based perovskites are being explored for flexible electronics, neuromorphic computing, and quantum devices. In this work, we investigated energy storage properties of Si-based $Cs_3Bi_2I_9$ perovskite for efficient use as MIM capacitor. $Cs_3Bi_2I_9$ was chosen as the model of this study due to several reasons. It is lead-free, efficient for addressing toxicity concerns unlike other materials such as $MAPbI_3$.[18] It is also a zero-dimensional layered material with isolated cluster of

---

[a] Applied Physics and Radiation Technologies Group, CCDCU, Faculty of Engineering and Technology, Sunway University, 47500 Bandar Sunway, Selangor, Malaysia. E-mail: yitas@sazu.edu.ng; mayeenk@sunway.edu.my

[b] Department of Physics, Sa'adu Zungur University, Gadau, Nigeria

[c] Department of Physics, College of Science, Korea University, 145 Anam-ro, Seongbuk-gu, Seoul, 02841, Republic of Korea

[d] Miyan Research Institute, International University of Business Agriculture and Technology, Dhaka-1230, Bangladesh

[e] Department of Industrial and Systems Engineering, College of Engineering, Princess Nourah bint Abdulrahman University, P.O. Box 84428, Riyadh 11671, Saudi Arabia

$(Bi_2I_9)^{3-}$, with high stability than 3D perovskites.[19] $Cs_3Bi_2I_9$ can also accept covalent elements to break symmetry easily and enhance polarization. Various reports also revealed that $Cs_3Bi_2I_9$ is highly stable under heat and humidity, applicable for real-world energy storage devices.[20]

2 Research method

All optimizations and calculations have been performed within the scope of density functional theory (DFT) implemented in quantum ESPRESSO and thermo_pw interface.[21] The pristine system of $Cs_3Bi_2I_9$ perovskite was generated from the materials project data base, with lattice parameters and coordinates based on the experimental alignments.[22] Consequently, the structure was fully relaxed, until the minimum energy on each atoms becomes 0.02 eV per atom. To obtain a balance between computational cost and accuracy, convergence criterion was followed by performing convergence tests (ecut and *K*_points).[23] For the ecut convergence, a converged value of 60 Ry was set up after running 20 Ry, 30 Ry, 40 Ry, 50 Ry, 60 Ry, 70 Ry and 80 Ry. Similarly, *K*_point converged value was set up at 9 × 9 × 9, after performing several *K*_point tests. Electronic and ionic interactions were determined using the generalized gradient approximation (GGA), in terms of Perdew–Burke–Emzerhop (PBE) norm-conserving pseudopotentials.[24] Because GGA underestimates band gap values, we employed DFT+U, in terms of Hubbard parameters, for the atoms with d' orbitals. Although, no literature supports adding U values of Cs and I atoms. Activating DFT+U in quantum espresso assists in obtaining relatively precise band gap values with U correction. Moreover, the U value of Si is chosen as zero because Silicon (Si) has no localized d or f electrons. It cannot be applied to s/p orbitals because it is main to correct strong on-site Coulomb interactions in localized d or f manifolds. Justification for U values in relation to the current work is shown in Table 1. To further screen the accurate band gap of the systems, hybrid HSE06 functional has also been used, and the results are compared with the GGA obtained ones.

To fabricate Si-based MIM leakage barrier, Si atoms were introduced into $Cs_3Bi_2I_9$ lattice in concentrations of 0.25 and 0.50 mol% respectively and the systems underwent relaxation again. To accurately assess the thermodynamic stability of Si substitution in $Cs_3Bi_2I_9$, the formation energy was computed using the standard defect-formation formalism referenced to elemental chemical potentials. For Si substituting Bi, the formation energy is given by[25]

$$E_f = E_{tot}(\mathrm{Si}) - E_{tot}(\mathrm{prisitne}) - \mu_{Si} - \mu_{Bi} \tag{1}$$

where $E_{tot}(\mathrm{Si})$ is the total energy of the relaxed Si-doped $Cs_3Bi_2I_9$ supercell, $E_{tot}(\mathrm{pristine})$ is the total energy of the undoped supercell, and μ_{Si} and μ_{Bi} are the chemical potentials of the respective atomic species. The elemental reference states are taken as: bcc-Cs(s), rhombohedral-Bi(s), $I_2(g)$ for iodine, and diamond-Si(s). To ensure thermodynamic stability, the chemical potentials are constrained by the $Cs_3Bi_2I_9$ stability condition:

$$3\mu_{Cs} + 2\mu_{Bi} + 9\mu_I = \Delta H_f(Cs_3Bi_2I_9) \tag{2}$$

with additional inequalities preventing decomposition into competing Cs–Bi–I secondary phases.

Electronic interactions, density of states and orbital interactions were determined from the density of state parameter[26]

$$g(E) = \frac{8\pi\sqrt{2}}{h^3} m^{\frac{3}{2}} \sqrt{E} - E_f \tag{3}$$

where *h* is the plank's constant. We analyze the charge polarizing parameter in terms of the born effective charges and charge density calculations. Polarization, electric field and dielectric behaviors of the systems were considered to fully understand the energy storage capacity of the MIM system under investigation.

The strained-induced charge storage properties of the systems were equally calculated by introducing 0.10% strain on the *z*-direction. Consequently, parameters such as piezoelectric coefficients, leakage and capacitance have been determined for the strain-induced systems.

3 Results and discussions

3.1 Structural parameters

Fig. 1(a) depicts a schematic layout of a typical MIM capacitor commonly used in microelectronics and energy storage.[27] The

Table 1 Electronic configurations and justification for DFT+U approach

Element	Electronic configuration/orbital	Recommended U (eV)	Justification
Cs	$1s^2\ 2s^2\ 2p^6\ 3s^2\ 3p^6\ 4s^2\ 3d^{10}\ 4p^6\ 5s^2\ 4d^{10}\ 5p^6\ 6s^1$	0.00	Cs d-states lie deeply within the core; previous reports on Cs-based halide perovskites never applies U to Cs
Bi	$1s^2\ 2s^2\ 2p^6\ 3s^2\ 3p^6\ 3d^{10}\ 4s^2\ 4p^6\ 4d^{10}\ 5s^2\ 5p^6\ 4f^{14}\ 5d^{10}\ 6s^2\ 6p^3$	0.00	Band edges are dominated by Bi 6p-statesd and are weakly correlated; most works use no U, some apply small U (<2 eV) to correct band gaps
I	$1s^2\ 2s^2\ 2p^6\ 3s^2\ 3p^6\ 3d^{10}\ 4s^2\ 4p^6\ 4d^{10}\ 5s^2\ 5p^5$	0.00	Halide p states are uncorrelated; no literature supports U on I in halide perovskites

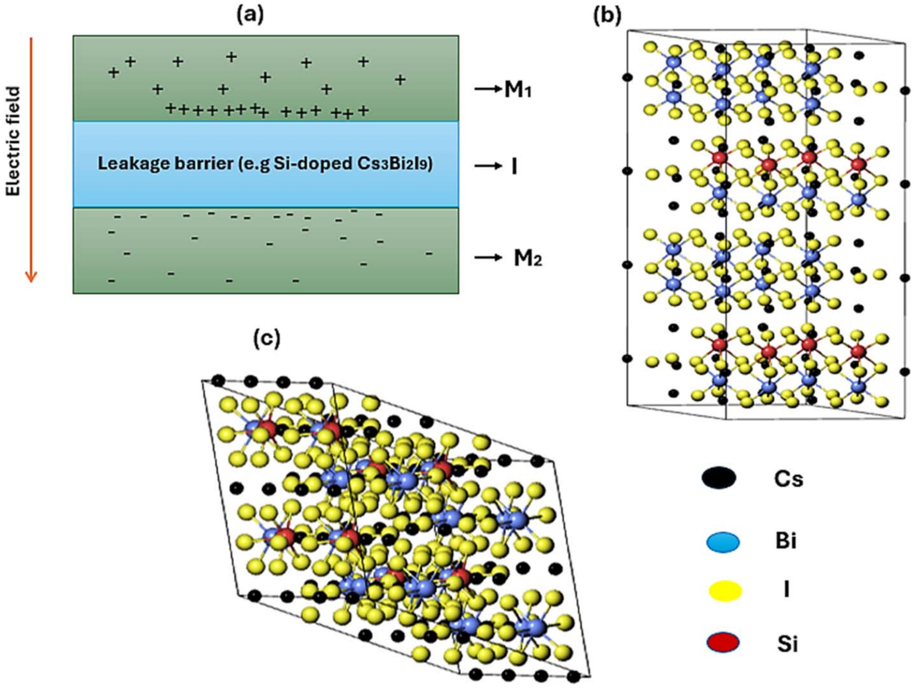

Fig. 1 (a) Schematic illustration of the Si based $Cs_3Bi_2I_9$ MIM capacitor, showing how electric field is set up due to voltage blockage in the leakage barrier (b) Si based $Cs_3Bi_2I_9$ crystal in *XY* viewed in *XY* plane (c) Si based $Cs_3Bi_2I_9$ crystal in *XYZ* viewed in *XY* plane.

top layer labeled M_1 acts as the positive terminal of the capacitor, which accumulates positive charges due to applied external voltage. The insulating layer (I) is the region which prevents leakage current by preventing direct charge flow. Otherwise, this dielectric layer stores excess energy by setting up electric field flow. On the other hand, M_2 acts as the second or negative terminal of the capacitor, which accumulates negative charges due to external voltage. As shown by the arrow direction, electric field is established across the insulator when external voltage is applied. The structural geometry of the Si based MIM capacitors are shown in Fig. 1(b and c), indicating *XY* and *XYZ* planes.

The original lattice of the pure $Cs_3Bi_2I_9$ perovskite was a hexagonal crystalline perovskite obtained from materials project data base. $Cs_3Bi_2I_3$ adopts a hexagonal $P6_3/mmc$ structure containing two distinct Cs^+ sites. In the first site, Cs^+ coordinates with twelve I^- ions in a CsI_{12} cuboctahedron that connects through corners and faces to neighboring CsI_{12} units and BiI_6 octahedra, with octahedral tilt angles of about 19° and Cs–I distances of 4.22–4.49 Å. The second Cs^+ site also forms a CsI_{12} cuboctahedron but with six shorter (4.27 Å) and six longer (4.37 Å) Cs–I bonds. Bi^{3+} forms BiI_6 octahedra exhibiting three short (2.96 Å) and three long (3.23 Å) Bi–I bonds. Two inequivalent I^- sites show 1- and 2-coordinate geometries. For the purposes of this work, a $2 \times 2 \times 2$ supercell containing 224 atoms was optimized based on lattice parameters $a = 8.54$ and $c = 2.16$ Å respectively.[28] Before relaxing, the original volume of the super cell model was 2732.54 $Å^3$. Later, the supercell was appropriately relaxed until the minimum energy per atom becomes 0.02 eV per atom. After relaxation, Pristine $Cs_3Bi_2I_9$ retained the centrosymmetric space group $P6_3/mm$, while 0.25 mol% Si-doped $Cs_3Bi_2I_9$ transformed to non-centrosymmetric space group $P6_3mc$. The observed transformation reveals loss of inversion symmetry due to asymmetric Si substitution within the Bi_2I_9 cluster.

Since Si^{4+} and Bi^{3+} are hetero-valent, doping with Si presented a relatively complex structure because Si^{4+} has smaller ionic radius than Bi^{3+} and Cs.[29,30] So, energy did not converge directly when Si substitutes Bi atoms. On this basis, the Si–Ti bonding process presented a significant lattice distortion with compensation by creating one positive charge (hole) according to

$$\mathrm{Si_{Bi}}^{4+} \rightarrow \mathrm{Bi_{Bi}}^{3+} + h \tag{4}$$

The lattice compensates this charge primarily through formation of iodine vacancy, which are the most common and lowest-energy compensating defects in halide perovskites. Therefore, the electronic and other properties obtained for Si-doped $Cs_3Bi_2I_9$ perovskites were based on iodine vacancy. The effects of 0.25 and 0.50 mol% Si atoms produced some decrease in the volume of the unit cell to 2645.78 and 2607.81 $Å^3$ respectively, because the ionic radius of Si atom is comparatively small to ionic radius of Bi atom. Bi–I bond length also elongates on the site of Si.[31]

To determine thermodynamic stability of the current systems, we considered formation energy parameter as shown in Table 2. Notably, Si substitution is energetically favourable within the full chemical-potential stability range of $Cs_3Bi_2I_9$. Under both I-rich and Bi-rich growth limits, the doped structures exhibit negative formation energies, confirming intrinsic thermodynamic stability. The 0.25 mol% Si configuration

Table 2 Structural parameters of the MIM systems under investigation

MIM systems	E_f (eV)	a; c (Å)	Volume (Å^3)
$Cs_3Bi_2I_9$	−0.96	8.54; 2.16	2673.44
0.25 mol% Si@$Cs_3Bi_2I_9$	−1.15	8.52; 2.15	2645.78
0.50 mol% Si@$Cs_3Bi_2I_9$	−1.20	8.49; 2.09	2607.81

remains the most stable, consistent with observed structural relaxation and reduced lattice volume.[32]

Additionally, the trend of the formation energy becomes more negative as Si concentration increases. Therefore, doping with Si leads to some thermodynamic stability especially in the 0.25 mol% variant. Slight decrease in lattice constants indicates lattice contraction due to smaller ionic radius of Si compared to Bi. Ultimately, the improved stability due to Si doping indicates a potentially good structural integrity under electric fields. On the other hand, reduced volume tightens the crystal lattice, which may lead to higher dielectric constants. On the overall notice, the progressive improvement from 0.25 to 0.50 mol% Si shows that controlled doping can tune material properties for optimal capacitor performance.

3.2 Initial electronic properties

Analyzing electronic properties of systems is highly significant in reporting their potential in MIM capacitor applications. For example, studying band gap parameters helps understand the materials metallicity, resistivity, work function and band alignment mechanisms necessary for efficient charge storage.[33] As presented in Fig. 2(a–c), the band structure diagrams for pure and Si-based $Cs_3Bi_2I_9$ variants identify important trends directly connected to properties of MIM capacitors, especially work function and band alignment. In the pure system, a wide band gap of 3.32 eV (3.47 eV with HSE06) suggests low intrinsic conductivity coupled with high voltage breakdown. This may lead to limitation in charge of injection efficiency. Significant band gap narrowing (2.70 eV GGA) and (2.82 with HSE06) were observed when 0.25 mol% Si atoms were introduced, which shows better charge carrier facilitation with improved polarization response. The corresponding band gaps for the 0.5 mol% Si-doped variants are (2.51 eV) and (2.59 eV) with GGA and HSE06 respectively. We also observed stronger electronic interaction due to additional Si atoms, which can influence materials dielectric behavior. Based on the information obtained in the band structure diagrams, presence of Si dopants in $Cs_3Bi_2I_9$ strategically regulates the band structure to optimize work function and band alignment. Collectively, this can tune to the material potential for high-performance MIM capacitors. Notably, 0.25 mol% Si-doped variant offers the best balance between electronic activity and dielectric stability.

The DOS diagrams presented in Fig. 3(a–c) revealed some number of electronic states available at various energy levels. As observed in Fig. 3(a), a clear indication of separation between valence band and conduction band emerged and relatively wide, indicating wide band gap in pure $Cs_3Bi_2I_9$. In Fig. 3(b) DOS peaks shifted slightly towards Fermi level, indicating band gap narrowing. Moreover, peaks near Fermi level shifted more and broader due to increase in Si concentration, as shown in Fig. 3(c). The mechanism of activities near Fermi level in the Si based $Cs_3Bi_2I_9$ MIM capacitors are subsequently explained using partial density of states (PDOS) analysis.

The PDOS pattern shown in Fig. 4(a–c) demonstrates various orbital activities in engineering electronic properties of the Si-based $Cs_3Bi_2I_9$ MIM capacitors. In Fig. 4(a), core energy levels (−12–−14 eV) are dominated by 5s (Cs) and 6s (Bi) orbitals. Therefore, core bands are primarily dominated by Cs 5s, Bi 6s, and I 5s orbitals, which can enhance stability and leakage suppression. As shown in Fig. 4(b), there is significant activity of p' orbitals of Si and Bi atoms near Fermi level. Also, Si p' state

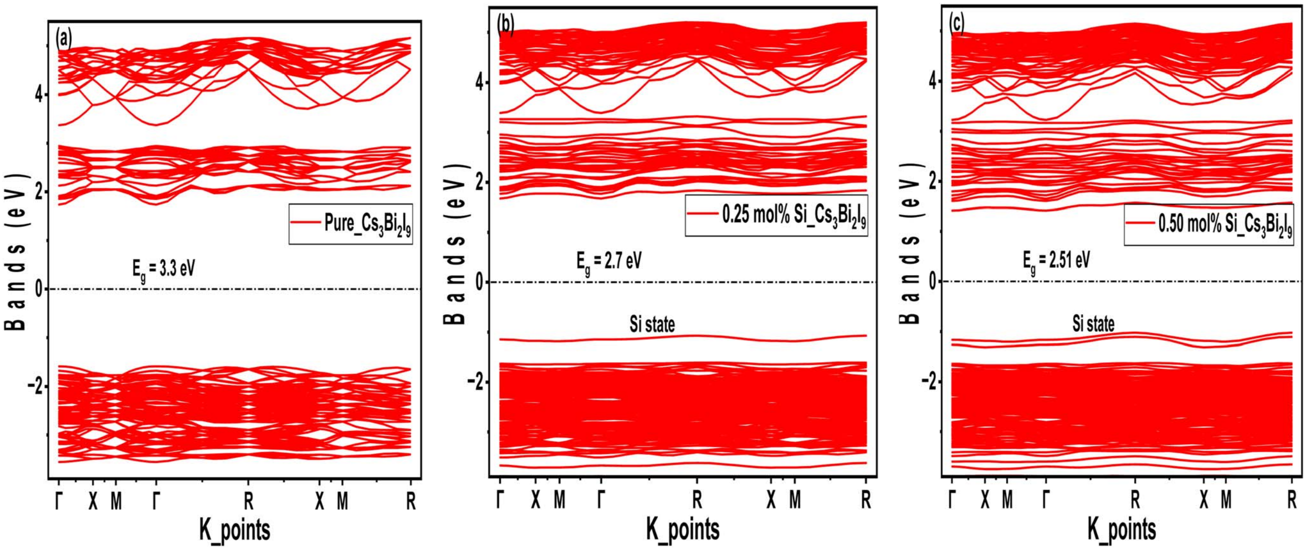

Fig. 2 GGA band structure diagrams of the $Cs_3Bi_2I_9$ MIM capacitor materials, each demonstrating energy bands at various energy levels (a) pure (b) 0.25 mol% Si (c) 0.50 mol% Si.

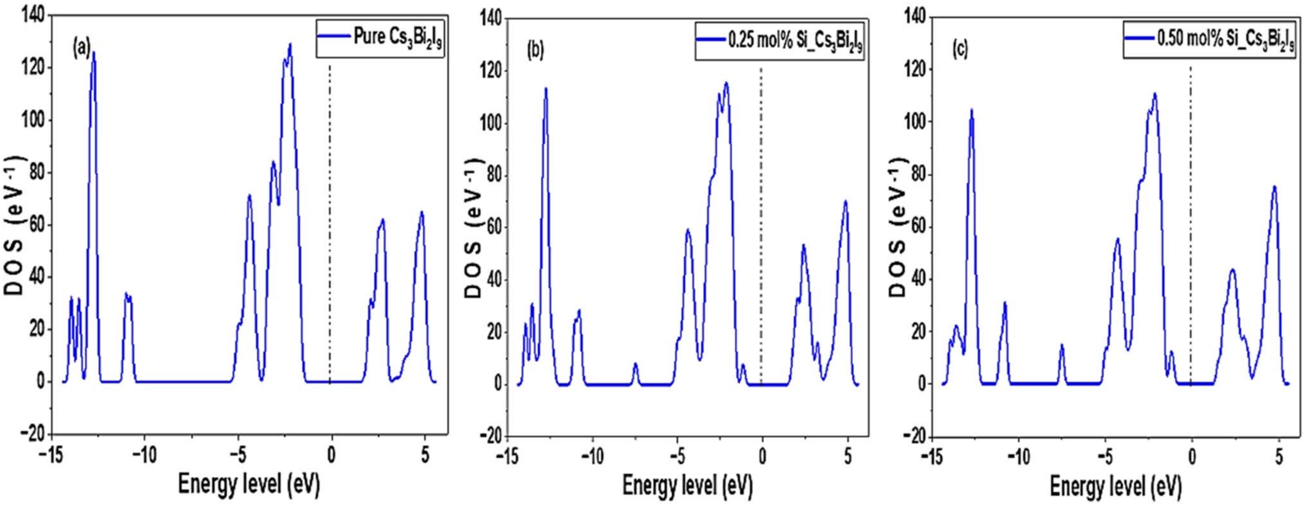

Fig. 3 DOS pattern of the $Cs_3Bi_2I_9$ MIM capacitor materials, each demonstrating the level of energy states occupations at various energy levels (a) pure (b) 0.25 mol% Si (c) 0.50 mol% Si.

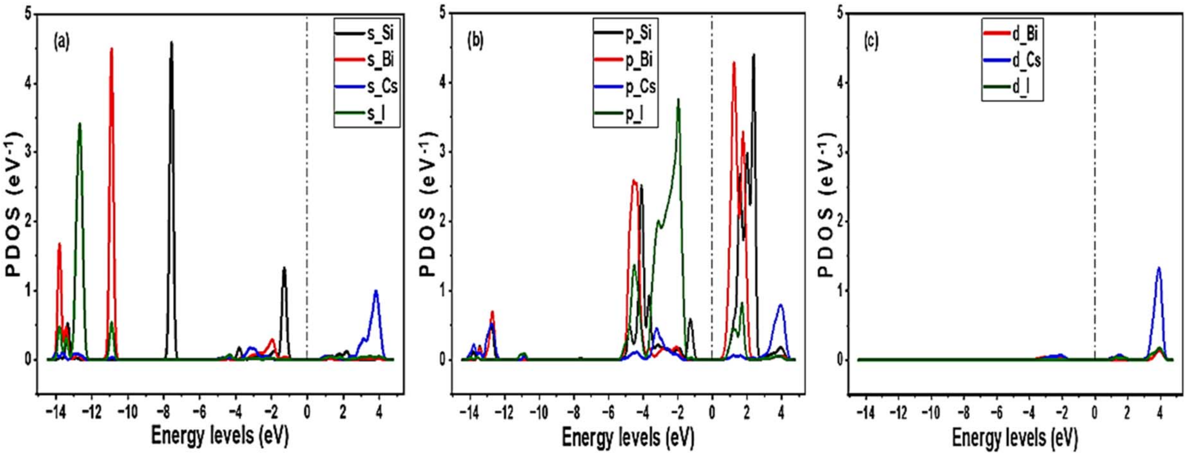

Fig. 4 PDOS pattern of the $Cs_3Bi_2I_9$ MIM capacitor materials, each demonstrating various orbital contributions at various energy levels (a) pure (b) 0.25 mol% Si (c) 0.50 mol% Si.

creates new state near CBM, which effectively narrows the band gap. Additionally, p′ orbitals of Bi and I contributed to the VBM, collectively forming the lower edge band gap. Notably in Fig. 4(c), d′ orbitals demonstrated minor contributions in the mid-gap state, hence considered less influential in the band gap formation.

3.2.1 Initial static dielectric constants.

Dielectric behavior of MIM systems relates their response to external electric fields across various energy levels.[34] In the current work, detailed discussions on the dielectric behaviors of $Cs_3Bi_2I_9$ MIM capacitors are done based on results referred in Fig. 5(a–c). In MIM capacitor, high and stable dielectric constant indicates improved charge storage and efficiency.[35] As shown in Fig. 5(a), pure $Cs_3Bi_2I_9$ revealed moderate response in the range 4–6 eV, suitable as a baseline insulator. However, its efficiency can be low due to strong polarization in the UV range. We observed enhanced dielectric response with 0.25 mol% system as shown in Fig. 5(b). Higher peak and broad energy range (2.5–5.4 eV) indicates increased polarization because of defect induced dipoles, localized lattice distortions and charge redistribution mechanism.[36] Notably, Si doping level (0.25 mol%) significantly improves energy storage efficiency with high chance of reduced leakage, relative to MIM capacitor applications. 0.5 mol% doping level (Fig. 5(c)) presented significantly modified profile with very little shift in the dielectric peak. The little shift in the dielectric peak suggests defect clustering with enhanced localized states. The overall mechanisms of dielectric response observed are due to electronic polarization (see Table 5) which is dominant at high frequencies; leading to band gap narrowing, which can increase carrier mobility and charge compensation mechanisms between Si^{4+} and Bi^{3+} ions. Based on our findings, 0.25 mol% Si-doped $Cs_3Bi_2I_9$ offers better balance between leakage control and dielectric enhancement.

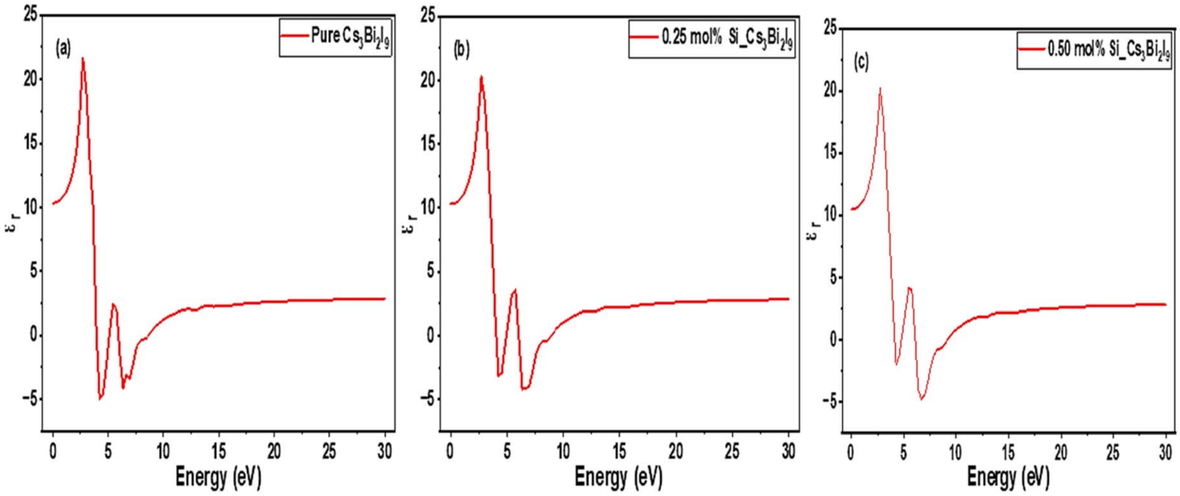

Fig. 5 Initial static dielectric constant spectra of $Cs_3Bi_2I_9$ MIM capacitor materials (a) pure (b) 0.25 mol% Si (c) 0.50 mol% Si.

Additionally, 0.5 mol% system may need careful defect control to prevent excessive leakage.

3.2.2 Born effective charge (BEC) distribution. BEC measures the change in crystal polarization when atom is displaced.[37] We analyse BEC distribution based on the calculated dielectric tensors, which reflects the dynamical activities of the electronic systems. Fig. 6(a–c) present BEC graph for pure and Si based $Cs_3Bi_2I_9$ MIM capacitor systems. The atomic indices for pure $Cs_3Bi_2I_9$ are: 2 = Cs; 3 = Cs; 4 = Cs; 5 = Cs; 6 = Cs; 7 = Si; 8 = Bi; 9 = Bi; 10 = Bi; 11 = I; 12 = I; 13 = I; and 14 = I; The corresponding atomic indices for 0.25 mol% and 0.50 mol% Si doped systems are obtained by replacing Bi index number (7) and (7 & 8) with Si atoms respectively. Fig. 6(a) depicts BEC tensor components of pure $Cs_3Bi_2I_9$ *vs.* atom indices in the range 2–14. Each line in the graph represents tensor components Z_{xx}, Z_{yy}, Z_{zz}, Z_{xy}, Z_{yx}, Z_{xz}, Z_{yz} and their mean values. Notably, all diagonal components presented directional polarization due to moderate values across indices 2–10. On the other hand, off diagonal components (Z_{xy}, Z_{yx}, Z_{xz}, Z_{yz}) demonstrate low anisotropic polarization. Primary polarizations are shown by indices 7–9 (Bi atoms), while indices 11–14 (I atoms) show negative charge values, efficient for charge compensation. Relatively constant mean charge values indicate low dynamic response in the pure $Cs_3Bi_2I_9$ perovskite. Generally, relatively stable BECs in pure $Cs_3Bi_2I_9$ reveals lower response to external fields.

In Fig. 6(b), Si atom (index 7) demonstrates a notable stronger diagonal component (Z_{xx}, Z_{yy} and Z_{zz}) indicating a higher local polarization. By introducing local polarization, there will be symmetry breaking and strong dipole formation, crucial for efficient dielectric performance. Indices 1–8 (Bi atoms) presented relatively high BEC values specifically in Z_{zz}

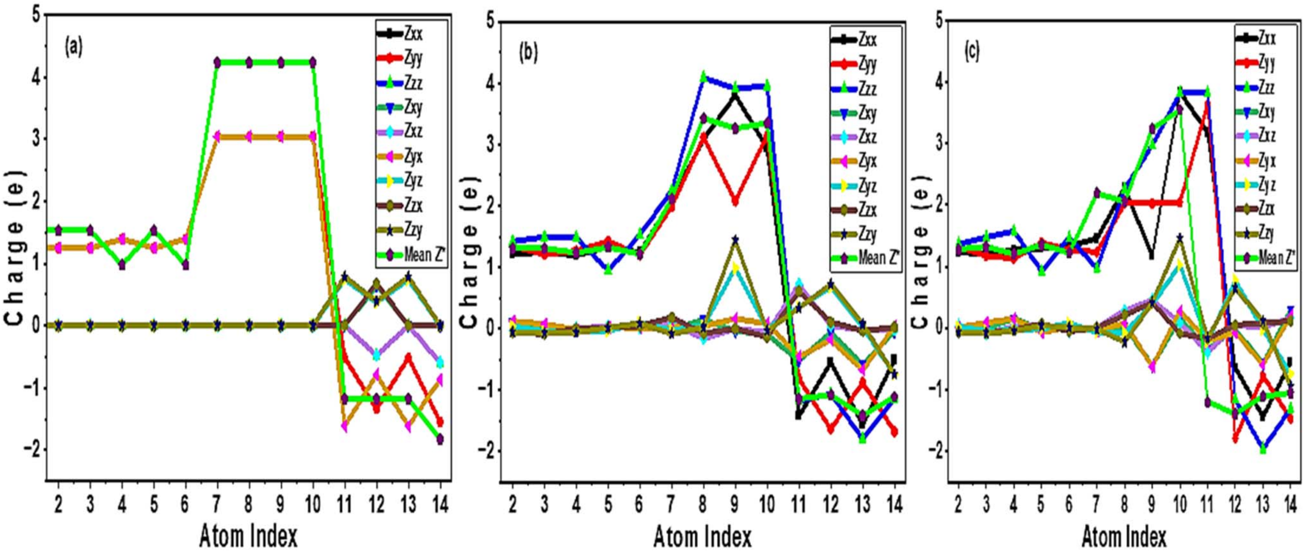

Fig. 6 Variation of BEC with atom indices of $Cs_3Bi_2I_9$ MIM capacitor materials (a) pure (b) 0.25 mol% Si (c) 0.50 mol% Si.

Table 3 BEC values of some high-level tensor components of the MIN capacitors under investigation

Systems	Z_{xx} (e)	Z_{yy} (e)	Z_{zz} (e)	Z_{xy} (e)	Z_{yz} (e)	Mean value (e)
Pure $Cs_3Bi_2I_9$	0.04957	0.04934	0.02819	−0.00000	−0.00000	−0.01680
0.25 mol% Si@$Cs_3Bi_2I_9$	−0.00562	−0.03521	−0.00958	0.02371	0.02411	1.34494
0.50 mol% Si@$Cs_3Bi_2I_9$	−0.00254	−0.03699	−0.00667	0.02645	0.00043	1.34577

and Z_{xx}. Indices 2–6 (Cs atoms) show medium and consistent BEC values efficient for supporting structural symmetry rather than taking role in active polarization. Charge compensation mechanisms are observed with indices 11–14 (I atoms) because of negative values of BEC, efficient for electrostatic stability and suppressing dielectric loss. The obtained high mean Z^* attributed to Si and Bi sites suggests strong dielectric activity, necessary for high-performance capacitors. Ultimately, adding 0.25 mol% Si in $Cs_3Bi_2I_9$ creates localized polarization centres and improves dielectric anisotropy, highly suitable for MIM capacitor materials where efficiency, miniaturization, and fast switching are critical. In the 0.50 mol% doped system, dual polarization centre emerged because of presence of more Si atoms. Therefore, there is highly distributed polarization coupled with stronger mean values and diagonal components. The dual-centre behaviour increases dielectric symmetry, which is significant for energy storage and minimizing local field concentration. As shown in Table 3, higher mean values for Si-doped systems confirmed strong response to polarization, while lower and negative mean value obtained from pure system suggest reduced net polarization. Therefore, the obtained BEC properties of pure $Cs_3Bi_2I_9$ inclined its application for non-tuneable high capacitance applications, while BEC properties attributed to Si-variants of $Cs_3Bi_2I_9$ suggests their application as tuneable capacitors, memory devices, or nonlinear dielectric applications.

3.2.3 Charge density distribution. The concept of charge density distribution enables better understanding of how electrons are distributed in $Cs_3Bi_2I_9$ and its Si doped variants.[38] It also highlights bonding characteristics, electronic interactions and centers of polarization. For better understanding of dielectric behaviors of these systems, we used charge density approach to identify regions of high and low electron localization and the significance of Si dopants. In the charge density diagram provided in Fig. 7(a), blue regions identify sparse electrons in the interstitial nonbonding regions. In the doped systems as shown in Fig. 7(b and c), it indicates where charges are pulled away because of polarization influence near Si site. Areas of high electron density are indicated by red zones. They typically represent active electronic environments and polarization centers.

Notably, pure $Cs_3Bi_2I_9$ perovskite reveals relatively uniform charge density distribution, showing high localized regions around Bi and I atoms. Due to this, the charge density distribution for this system suggests stable electronic environment with well-defined bonding. There is significant charge enhancement near Si site in the 0.25 mol% system due to presence of single red region, which is efficient for improving dielectric properties. We also observed slight asymmetry due to presence of Si atoms, confirming local distortion and incrased dipole moments.[39] By increasing Si concetration to 0.50 mol%, charge density becomes more intense around Si atoms. For example, two distinct red regions appeared near both Si atoms, signifying improved and spread charge localization. The system also shows greater anisotropy leading to high field response.

3.3 Unstrained mechanical properties

Describing mechanical parameters such as shear moduli and Poisson's ratio can explain mechanical stability and how dielectric materials respond to voltage induced mechanical stress.[40] Based on the related previous data, optimum balance between electrical and mechanical properties leads to performance consistency.[41] A 3D visualization of the shear moduli for $Cs_3Bi_2I_9$ MIM capacitors under investigation is presented in Fig. 8(a–c), according to the relation[42]

$$G = \frac{\tau}{\gamma} \tag{5}$$

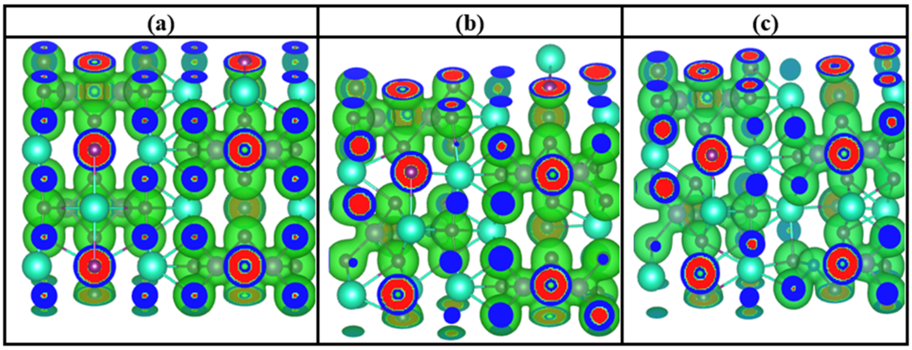

Fig. 7 Charge density distribtion of $Cs_3Bi_2I_9$ MIM capacitor materials (a) pure (b) 0.25 mol% Si (c) 0.50 mol% Si.

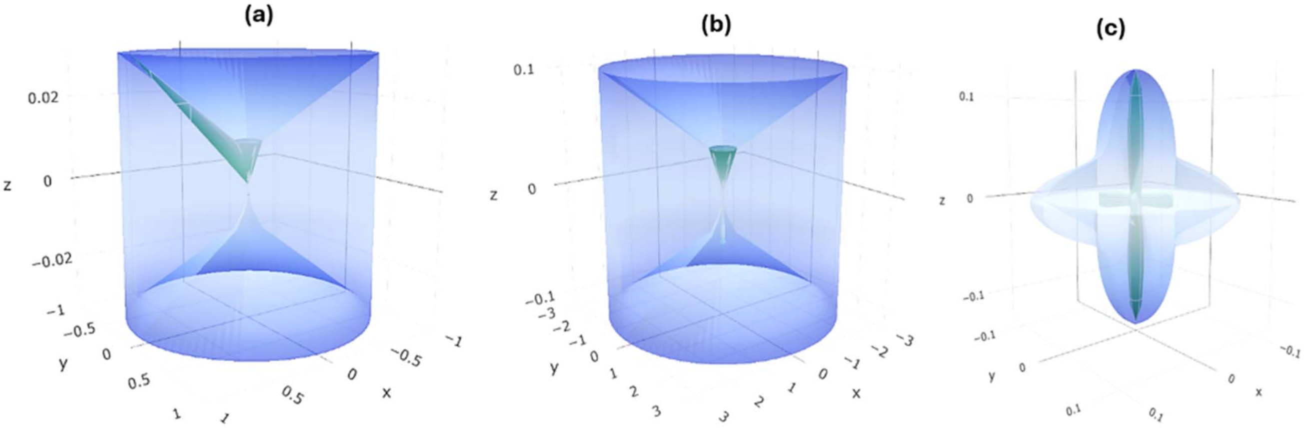

Fig. 8 Spacial dependence of shear moduli of $Cs_3Bi_2I_9$ MIM capacitor materials (a) pure (b) 0.25 mol% Si (c) 0.50 mol% Si.

Table 4 Tensile properties of the $Cs_3Bi_2I_9$ MIM capacitors

	Y (GPa)		*G* (GPa)		(*P*)	
MIM systems	Min	Max	Min	Max	Min	Max
Pure $Cs_3Bi_2I_9$	0.003999	183.65	0.001	66.4	0.0000038	0.99998
0.25 mol% $Si@Cs_3Bi_2I_9$	0.014239	137.27	0.00356	50.195	0.0000037	0.99992
0.50 mol% $Si@Cs_3Bi_2I_9$	0.011259	0.19804	0.00291	0.12518	−1.6218	2.0873

where τ is the shear stress and γ is the shear strain. A cylindrical shape with green surface intersecting the cylinder indicates unifiom shear modulus across directions. A slight asymmety was observed in Fig. 8(b), specifically along *z*-direction. The green surface is titled more than in Fig. 8(a), showing the emergence of anisotropy. Hence Si atoms intoroduced directional dependence stiffness bacause of lattice distortions. Ellipsoidal pattern shows stronger anisotropy in Fig. 8(c), which is also confirmed by intersecting planes along *x*, *y* and *z*-axies. Acoording to Liang *et al.*, anisotopy is significant for nonlinear dielectric materials but requires good management under high electric fields.[43] The tabulated calculated values of the directional dependence mechanical properties of the current systems are shwon in Table 4. Notably, highest values of stiffnesss, shear moduli and Poisson's ratio values are typical for pure $Cs_3Bi_2I_9$. Although good for structural stability, low stiffness is necessary for flexible MIM capacitors. Ehanced flexibility was observed in 0.25 mol% Si-based system, due to reduced

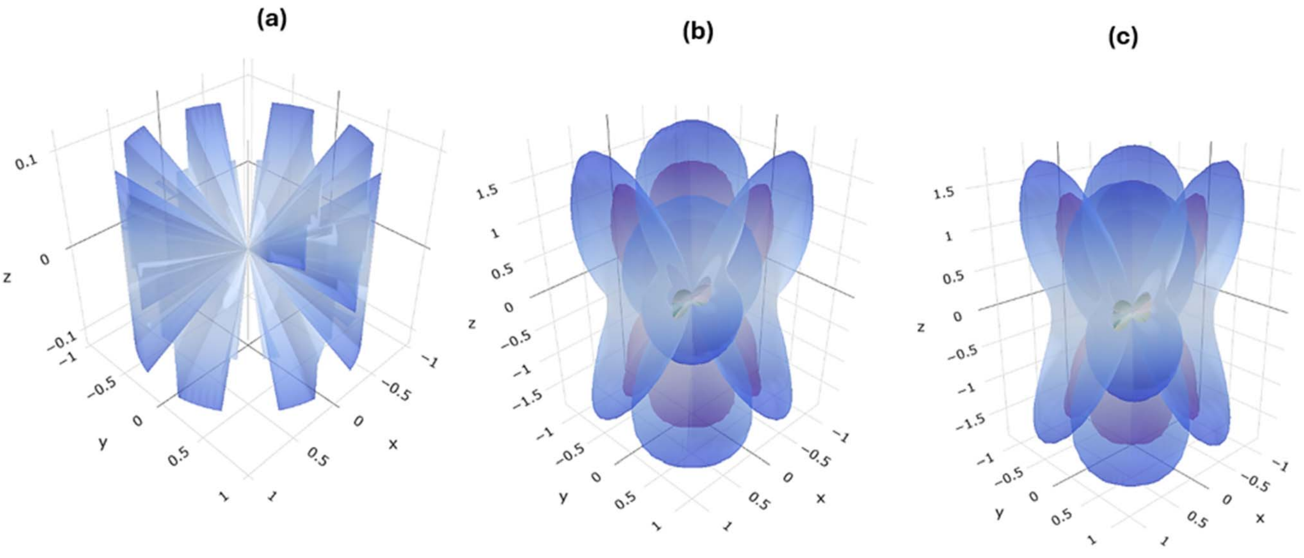

Fig. 9 Spacial dependence of Poisson's ratio of $Cs_3Bi_2I_9$ MIM capacitor materials (a) pure (b) 0.25 mol% Si (c) 0.50 mol% Si.

values of stiffness and shear moduli. The 0.50 mol% MIM system is extremely mechanically soft. With careful mechanical design, it can be useful for strain sensitive electronics.

In Fig. 9(a), highly symmetric pattern of Poisson's ratio confirms isotropic response. Therefore, pure $Cs_3Bi_2I_9$ responds uniformly under mechanical stress. However, anisotropic response was confirmed as shown in Fig. 9(b), due to apperance of irregular overlapping lobes caused by 0.25 mol% Si atoms. This observed behaviours can influence stress distribution in the dielectric layer, potentially influencing dielectric breakdown or fatigue resistance. Accroding to Fig. 9(c), the 0.50 mol% Si-based MIM system shows a moderately symmetric property, suggesting a patically restored symmetery. The behavoiur attributed to this system ehnaced its mechanical compliance necessary to maintain electrical performance.

3.4 Initial dielectric constant, electric field and polarization tensors

In the concept of MIM capacitor materials, we provided highlights of how Si atoms influences dielectric properties of $Cs_3Bi_2I_9$ perovskite. We determine the capacitance of the MIM sysrems under investigation from the expression[44]

$$C = \varepsilon_0 \varepsilon_r \frac{A}{d} \tag{6}$$

where A and d respresent area and thickness of the parallel metal electrodes in the MIM systems. ε_r is the relative permittivity obtained form the dielectric tensor data from Table 4. We also determined electric field strength of the corresponding MIM systems by assuming electric dipslacement field $D = (1, 1, 1) \times 10^{-12}$ Cm^{-2}, according to the formular[45]

$$E = \frac{1}{\varepsilon_0 \varepsilon_r} D \tag{7}$$

Based on the calcualted values in Table 5, capacitance (C) is directly proportional to dielectric constants. Notably, there is high increase in ε values due to introduction of Si impurities, leading to higher capacitance. On the other hand, E was inversely proportional to ε values in all anisotropic directions. As ε increase, there is corresponding decrease in the E values required to maintain same charge displacement. Based on previous reports, the observed phenomena is necessary for low leakage risks and better riliability.[46] Pure $Cs_3Bi_2I_9$ demonstrates the lowest C and E values, whereas 0.50 mol% Si based variant reveals highest C and relatively reduced E values compared to 0.25 mol% Si based variant, which is an indication of dielectric screening, ideal for high performance MIM capacitors.[47] To determine polarization effects, we adopt expression of polarization to electric field as presented in eqn (8)

$$E_i = \frac{1}{\varepsilon_0 \varepsilon_r} P_i \tag{8}$$

where ε_0 is the vacuum permittivity space (8.854×10^{-12} F m^{-1}) and ε_r is the relative permittivity. Calculation was done using the modern Berry-phase formalism, which correctly yields zero polarization for centrosymmetric pristine $Cs_3Bi_2I_9$ and finite polarization only for doped structures with verified non-centrosymmetric symmetry. To determine whether Si doping induces global symmetry breaking necessary for ferroelectric or piezoelectric behavior, we performed full point-group and space-group analysis using the spglib implementation in Thermo_pw. The emergence of finite macroscopic polarization and non-zero piezoelectric tensors in the Si-doped systems is therefore fully consistent with the observed global symmetry breaking. Data from the microscopic dipole distribution (Table 6) due to Si-doping in $Cs_3Bi_2I_9$ reveals a clear alignment with the enhanced dielectric response previously observed. In the pristine system, there is negligible out-of-plane (z-direction) contribution, consistent with the centrosymmetric nature of the $P6_3/mmc$ phase, prohibiting spontaneous polarization. When 0.25 mol% Si were introduced, the z-component increases from near zero to approximately 7.46 e·Å, corresponding to 0.0447C m^{-2}. This increase confirms that substitutional Si breaks the local inversion symmetry within the Bi_2I_9 polyhedral units by inducing asymmetric charge redistribution and selective bond shortening. This collectively promote off-cantering of both cations and anions. Moreover, these microscopic distortions

Table 5 Dielectric tensors and energy storage deriven paramters of the cureent $Cs_3Bi_2I_9$ MIM capacitors

Systems	ε_{xx}	ε_{yy}	ε_{zz}	C_{xx}; C_{yy}; C_{zz} (μF cm^{-2})	E_{xx}; E_{yy}; E_{zz} (Vm^{-1})
Pure $Cs_3Bi_2I_9$	4.02	4.02	4.23	3.75; 3.75; 3.55	3.69; 3.69×10^{-7}; 1.08×10^{-9}
0.25 mol% Si@$Cs_3Bi_2I_9$	5.09	5.09	4.66	4.51; 4.51; 4.13	2.22×10^{10}; 2.22×10^{10}; 2.42×10^{10}
0.50 mol% Si@$Cs_3Bi_2I_9$	5.22	5.22	4.79	4.62; 4.62; 4.24	2.16×10^{10}; 2.16×10^{10}; 2.36×10^{10}

Table 6 Comparison of dipole vectors and polarization for pristine and Si-doped $Cs_3Bi_2I_9$, showing how substitutional Si introduces and amplifies local polar distortions that drive enhanced dielectric and polarization responses

MIM systems	μ (e.Å)	μ (Debye)	$\sim P$ (Cm^{-2})
Pure $Cs_3Bi_2I_9$	(−8.4283, −14.5982, ∼0)	(−40.48, −70.12, ∼0)	(−0.05046, −0.08740, ∼1.7×10^{-9})
0.25 mol% Si@$Cs_3Bi_2I_9$	(−4.2141, −12.1652, 7.4626)	(−20.24, −58.43, 35.84)	(−0.02523, −0.07283, 0.04468)
0.50 mol% Si@$Cs_3Bi_2I_9$	(−4.2141, −7.2991, 21.7287)	(−20.24, −35.06, 104.37)	(−0.02523, −0.04370, 0.13009)

align with the enhanced Born effective charges and charge-density asymmetries reported earlier in the manuscript.

The effect becomes significantly amplified with 0.5 mol% Si. The z-dipole rises to 21.73 e Å, more than the magnitude observed in the 0.25 mol%-Si case, producing polarization of approximately 0.13C m^{-2}. This pronounced increase highlights the cooperative nature of Si-induced polar distortions: multiple Si sites reinforce each other through lattice-mediated long-range electrostatic interactions, driving stronger symmetry breaking across the supercell. Meanwhile, the in-plane dipole components systematically decrease, suggesting partial recovery of lateral symmetry even as vertical asymmetry intensifies. Collectively, these trends demonstrate that Si substitution introduces robust polar centres, offering a compelling microscopic explanation for the experimentally relevant enhancement of dielectric, polarization, and piezoelectric properties in Si-doped $Cs_3Bi_2I_9$.

Fig. 10(a–d) present a graphical visualization of the components of dielectric tensors, capacitance and electric fields. Fig. 10(a) indicates the existence of linear relationship capacitance and dielectric tensor in x-direction, indicating that more energy per unit voltage is stored according to theoretical equation

$$C = \varepsilon_0 \varepsilon_r \frac{A}{d} \tag{9}$$

z-tensor component also shows increasing trend with non-linear deviation at higher dielectric values, indicating saturation in z-direction due to structural distortion by Si atoms. In Fig. 10(d), linear variation between polarization and electric field suggests field-induced polarization, aligning with field strength. It shall be noted that properties in y-direction are not reported because x- and y-directions are isotropic (see Table 5)

3.5 0.10% strained energy storage analysis

The concept of strained energy storage properties of the current systems under study cannot be overlooked. Applying external strain to energy storage materials modifies orbital overlap and charge distribution, which boosts their dielectric response.[48] Strained electronic devices also exhibit better piezoelectric properties due to increased polarization.[49] However, applying strain requires very careful procedure because excess strain can compromise the system's mechanical stability. In the current study, we applied 0.10% strain on the z-direction of the three $Cs_3Bi_2I_9$ MIM systems and subsequently observe changes in various energy storage parameters such as band gap, charge

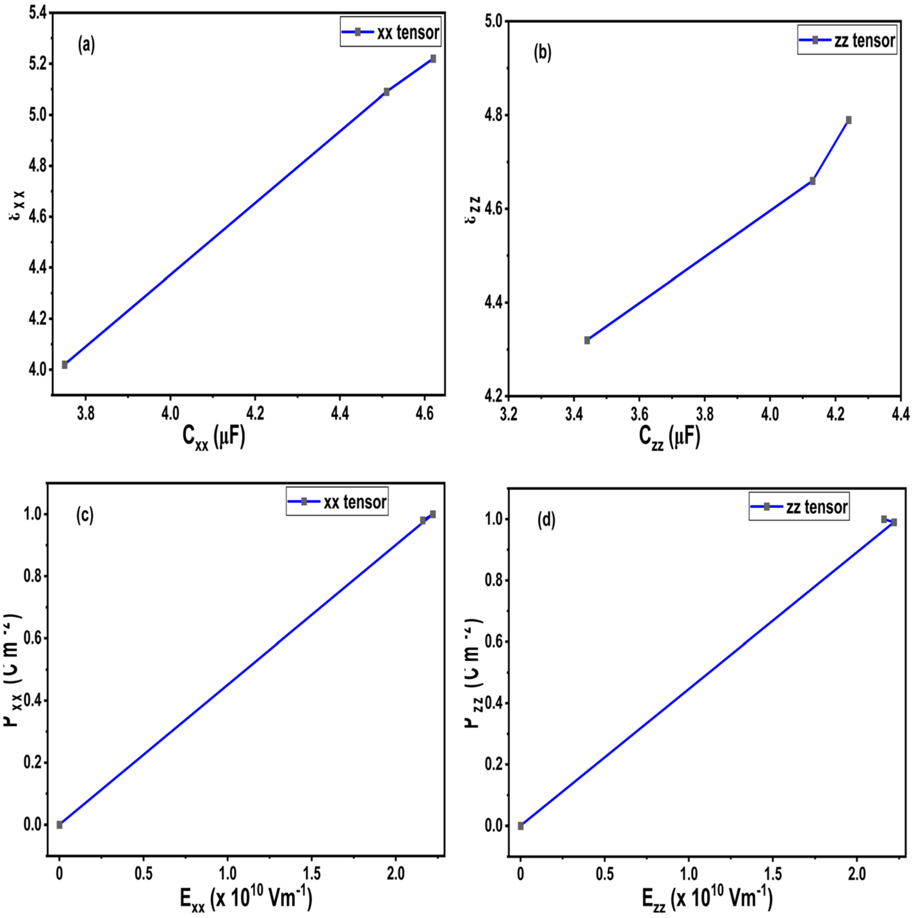

Fig. 10 Variation of capacitance with dielectric constants (a) x-direction (b) y-direction. Variation of electric field with polarization (c) x-direction (d) y-direction. The plotted graphs are based on the calculated values of Tables 4 and 5.

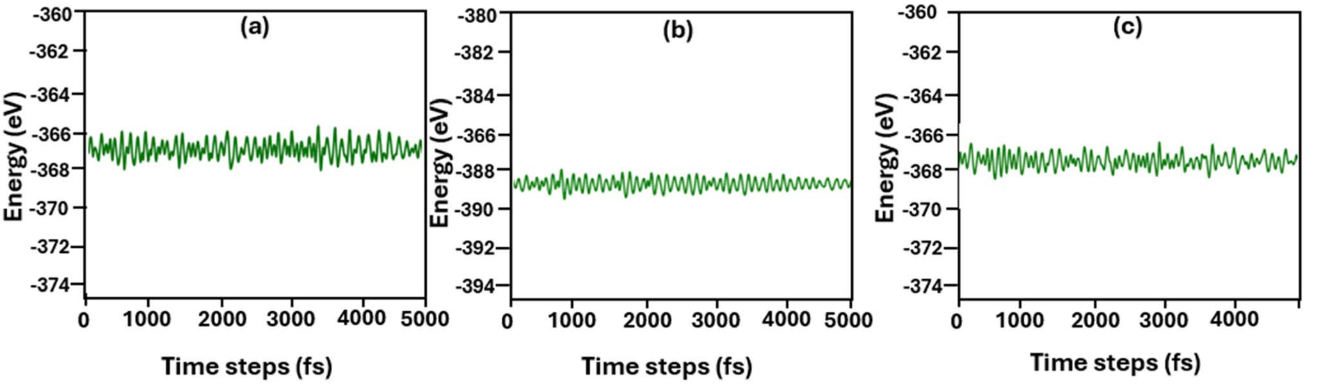

Fig. 11 Energy variations for the $Cs_3Bi_2I_9$ perovskite and its Si-doped variants under 300 K. (a) Pure (b) 0.25 mol% Si-doped (c) 0.50 mol% Si-doped.

density, polarization, electric field and piezoelectric response. The *ab initio* molecular dynamics (AIMD) results for pure and doped $Cs_3Bi_2I_9$ systems are displayed in Fig. 11(a–c). results have been achieved by performing AIMD simulations at 300 K under the condition $x = 2$. In all three systems, the total energy exhibit only minor fluctuations throughout the simulation, indicating strong thermal stability of the structures, consistent with previous findings.[50] Maintaining structural integrity at 300 K is particularly important, as it demonstrates that the investigated $Cs_3Bi_2I_9$ systems can operate safely under typical capacitor operating conditions.

3.5.1 Strained electronic properties. To align with the concept in this research work, we take account of the changes on the electronic properties after introducing 0.10% strain along *z*-direction. According to some reports, strain induced electronic systems undergo significant change in polarization and charge storage capacity.[51,52] Fig. 12(a–c) display the obtained strained electronic band structures of the $Cs_3Bi_2I_9$ MIM systems under investigation. Compared to initial systems (refer to Section 3.2), we observed slight narrowing and broadening in band gap due to stress-induced shift of some energy bands. For example, the initial band gap of the pure $Cs_3Bi_2I_9$ which was 3.3 eV, is slightly narrowed to ∼3.2 eV after 0.10% strain was induced to the system. The observed band gap value has brought $Cs_3Bi_2I_9$ to moderate insulation and low leakage range, ideal for high-performance MIM capacitors.[53] Although its band gap decreased, the probability of excessive leakage is still low since band gap is still wide. In Fig. 12(b and c), 0.25 mol% Si based $Cs_3Bi_2I_9$ experienced some widening of band gap, to new value of ∼2.8 eV, while some decrease to ∼2.4 eV is attributed to 0.50 mol% Si based $Cs_3Bi_2I_9$. At low Si content, strain slightly decreases the lattice distortion and enhances orbital alignment, which in turn reduces some defects states and restore symmetry.[54] With this, the conduction band and valence band are pushed apart, leading to increase in band gap. Since lattice is already distorted with 0.25 mol% Si, introducing more Si

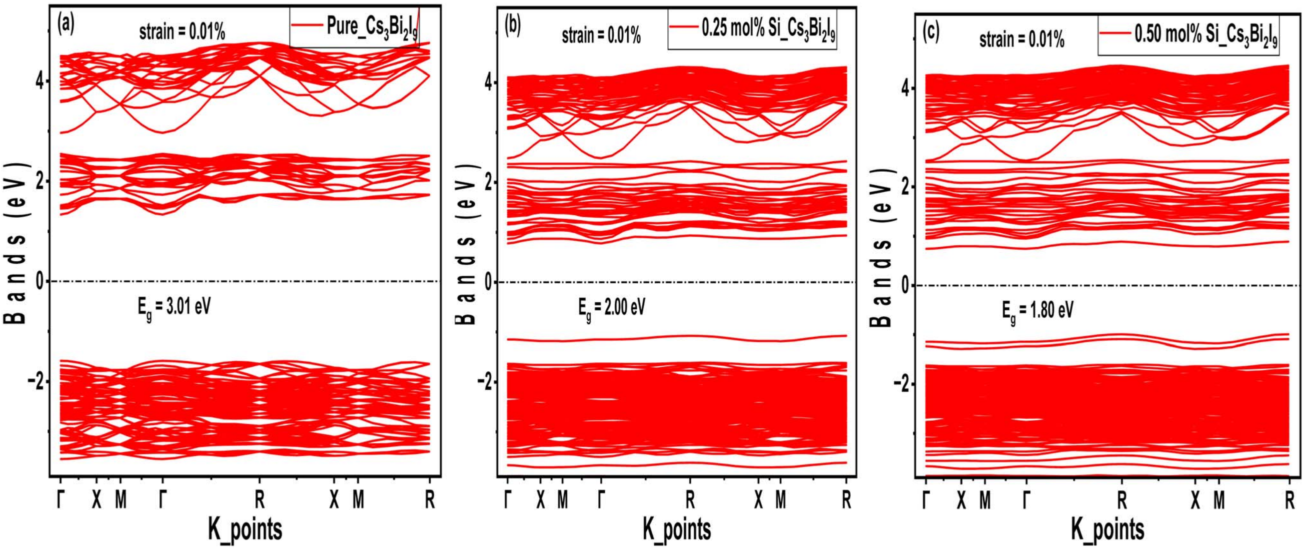

Fig. 12 0.10% strained band structure diagrams of the $Cs_3Bi_2I_9$ MIM capacitor materials, each demonstrating energy bands at various energy levels (a) pure (b) 0.25 mol% Si (c) 0.50 mol% Si.

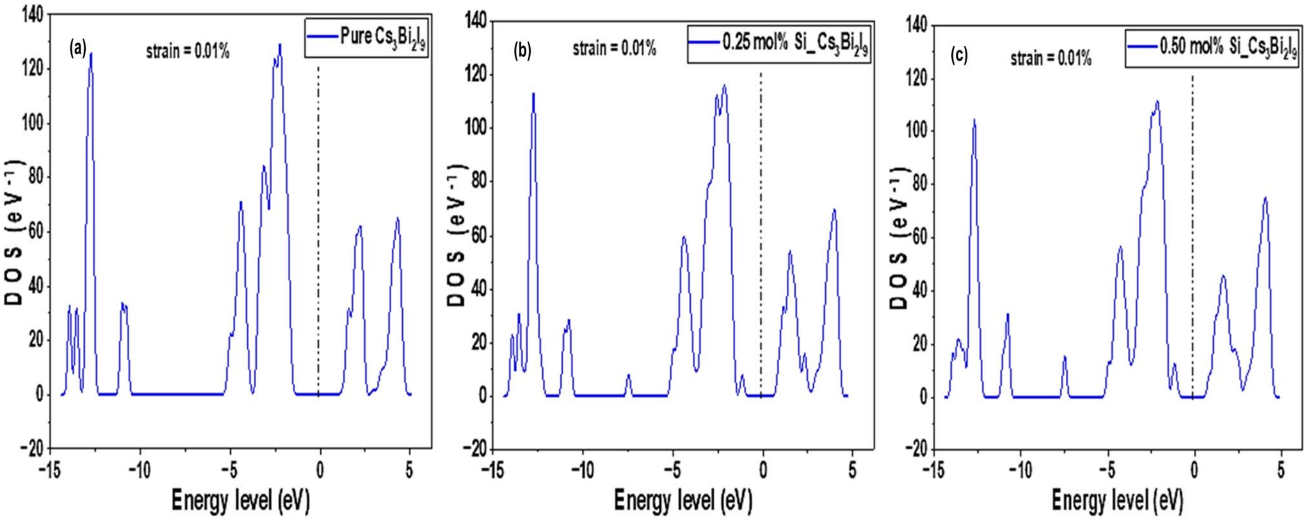

Fig. 13 0.10% strained DOS pattern of the $Cs_3Bi_2I_9$ MIM capacitor materials, each demonstrating the level of energy states occupations at various energy levels (a) pure (b) 0.25 mol% Si (c) 0.50 mol% Si.

concentration with 0.10 strain increases hybridization between Si 3p and Bi/I p orbitals, which pulls bands closer due to high electronic disorder within mid-gap states. Based on the results implications, 0.25 mol% can provide a balanced performance with low leakage and improved stability than 0.50 mol% Si based system. More discussion on leakage can be found under Section 3.10.

The corresponding strained DOS diagrams of these systems are shown in Fig. 13(a–c), each confirming some semi-conducting properties of the strained systems. According Guancheng *et al.*, static dielectric constants of perovskites are highly sensitive to structural deformations and redistribution of electronic density.[55] As shown in Fig. 14(a–c), all spectra exhibited relatively sharp peaks at low energy despite undergoing strain. In Fig. 14(a), we observed minimal change in dielectric spectra because $Cs_3Bi_2I_9$ remains largely centrosymmetric. Abrupt drop in the peak to near zero suggests limited polarizability and weak dielectric response under strain.[56] This is because of the centrosymmetric structure, which suppresses ionic displacement during strain. The peak of 0.25 mol% Si system rise to new high intensity and then becomes broader at low energy region, suggesting enhanced polarizability (see polarization). In Fig. 14(c), peak maintains highest value with greater fluctuations due to high anisotropy, which may also indicate some instability due to effects of excess Si atoms and strain.

Effects of mechanical strain on the charge density distribution were also considered as shown in Fig. 15(a–c). Compared to the initial systems (see Fig. 7), there is noticeable increase in charge overlap particularly the doped systems, which is an indication of stronger strain-induced polarization. In the pure system, there is high localization with minimum overlap around Si atoms, indicating some covalent interactions. We also noticed increased overlap on the Bi–I and Si-related regions

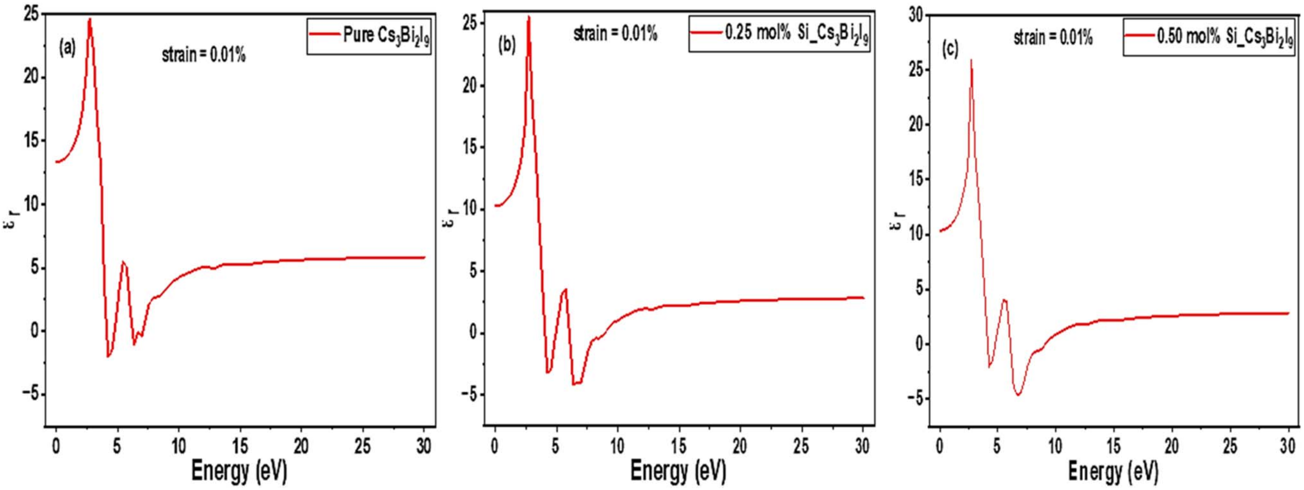

Fig. 14 0.10% strained static dielectric constant spectra of $Cs_3Bi_2I_9$ MIM capacitor materials (a) pure (b) 0.25 mol% Si (c) 0.50 mol% Si.

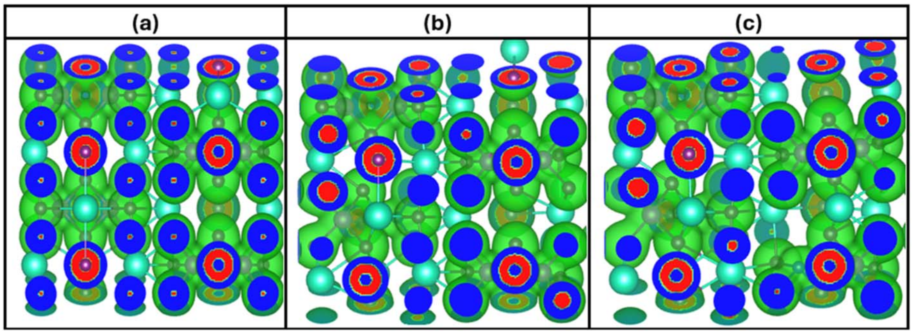

Fig. 15 0.10% strained charge density distribtion of $Cs_3Bi_2I_9$ MIM capacitor materials (a) pure (b) 0.25 mol% Si (c) 0.50 mol% Si.

of the 0.25 mol% Si system. This is because induced strain creates mechanism that breaks symmetry and introduces some localized states. Charge distribution is more distorted in 0.50 mol% Si system. However, proper mechanisms must be adopted to prevent leakage.

3.5.2 Strained piezoelectric coefficients, polarization and dielectric loss tangent (tan δ). Strained piezoelectric coefficient explains how much charges are generated due to mechanical stress. Low values indicate system's low response to mechanical deformation and produce very little charge when compressed, stretched, or bent.[57] Systems with these properties exhibit poor electrochemical coupling. On the other hand, high values indicate improved charge generation mechanism and sufficient energy conversion efficiency. As shown in Table 7, pure $Cs_3Bi_2I_9$ reveals negligible piezo electric coefficients, suggesting minimal influence of mechanical strain on charge displacement mechanism, which suppresses its potential as strain-sensitive MIM capacitor material such as sensors. Therefore, it can be regarded as showing low tunability with inefficient electrochemical coupling. Strong out-of-plane piezoelectricity was observed attributable to 0.25 mol% Si-doped system in the *z*-direction, which can enhance charge accumulation and lateral strain, ideal for flexible electronics, strain sensors, and energy harvesting devices. In the 0.50 mol% Si-doped system, results indicate strong vertical polarization due relatively high values of piezoelectric parameters in all directions. This is typical for 0D MIM materials, where vertical charge displacement improves capacitance modulation and strain-tunable dielectric characteristics.

Data from Table 8 show how 0.10% strain regulates polarization properties of the $Cs_3Bi_2I_9$ MIM energy storage systems. Polarization in pure $Cs_3Bi_2I_9$ remains significantly low, aligning with with piezoelectric response already discussed. Findings aligns well with Sun *et al.*,[58] who identified near-zero polarization because of the centrosymmetric nature and weak ionic displacement. In the 0.25 mol% system, polarization is slighly increased, which is well known for energy storage materials. For the 0.50 mol% system, the induced strain amplified polarization in the *z*-direction because of strain regulated properties.

To complete this study, it is necessary to address the anticipated leakage of the systems under study. In the context of this work, we consider leakages in terms of the dielectric loss tangent. It is defined as the conduction losses due to leakage currents in the MIM capacitor systems.[60] High values of tan δ signify excess loss while low values result to improved performance due to low conduction losses. We discussed the parameter of tan δ based on the relation[61]

Table 7 Piezoelectric coefficients of the strained $Cs_3Bi_2I_9$ MIM capacitors

MIM systems	d_{xx} (Cm^{-2})	d_{yy} (Cm^{-2})	d_{zz} (Cm^{-2})	Remarks
Pure $Cs_3Bi_2I_9$	1.00×10^{-8}	-1.32×10^{-13}	-4.01×10^{-16}	Piezoelectric response is negligible
0.25 mol% $Si@Cs_3Bi_2I_9$	20.00	20.00	50.00	Strong out-of-plane anisotropy and piezoelectricity
0.50 mol% $Si@Cs_3Bi_2I_9$	40.00	40.00	50.00	Improved out-of-lane piezoelectric response and anisotropy

Table 8 Polarization properties of the MIM capacitors under investigation, compared with previous experiments

	Polarization				
Systems	P_{xx} (Cm^{-2})	P_{yy} (Cm^{-2})	P_{zz} (Cm^{-2})	Remarks	Previos works and reference
Pure $Cs_3Bi_2I_9$	1.33×10^{-10}	∼0	∼0	Strain intorduced negligible effect	∼0 by Sun *et al.*[58]
0.25 mol% $Si@Cs_3Bi_2I_9$	1.005	1.005	0.990	Strain slightly increased polarization, remains strong dielectric	0.95 by Adams *et al.*[59]
0.50 mol% $Si@Cs_3Bi_2I_9$	0.984	0.984	1.005	Anisortropy is more under this strain	0.97 by Adams *et al.*[59]

Table 9 Leakage values of the intrinsic and strained $Cs_3Bi_2I_9$ MIM systems under investigation

MIM systems	Initial tan δ (Am^{-2})	Strained tan δ (Am^{-2})	Remarks	Obtained results from related works
Pure $Cs_3Bi_2I_9$	0.20	0.18	Strain slightly reduces dielectric loss, improving efficiency and stability	Sun *et al.* reported improved dielectric behaviour with anisotropic properties under strain[62]
0.25 mol% Si@$Cs_3Bi_2I_9$	0.22	0.19	Optimal doping: strain lowers loss tangent, enhancing energy storage and reliability	Liu *et al.* showed that strain reduces dielectric loss at 0.25% but failed to provide values[63]
0.50 mol% Si@$Cs_3Bi_2I_9$	0.24	∼0.3	Excessive Si doping under strain increases dielectric loss, risking leakage and instability	Kastuar and Ekuma mentioned that showed that excessive strain leads to mechanical instability and increased dielectric loss, especially in soft 2D $Cs_3Bi_2I_3$ structures[64]

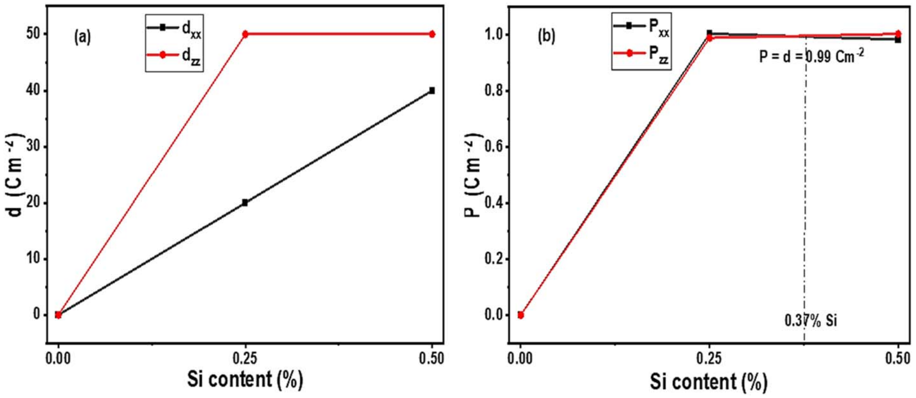

Fig. 16 Effects of Si concentration on (a) piezoelectric coefficients (b) polarization, for the $Cs_3Bi_2I_9$ MIM systems.

$$\tan\ \delta = \frac{\varepsilon_i}{\varepsilon_r} \tag{10}$$

where ε_i and ε_r are the imaginary and real dielectric permittivity respectively. As shown in Table 9, initial tan δ is the baseline conductivity loss for the untrained systems. Pure $Cs_3B_2I_9$ presented significantly lowest loss, while Si doping slightly increases loss due to increased polarization. Introducing 0.10% strain generally lowers loss for pure and 0.25 mol% doped systems, indicating improved performance. The reduced conductivity loss attributable to pure $Cs_3Bi_2I_9$ is due to low strain-induced polarization, while slightly increased loss in 0.25 mol% is because of increased strain-induced polarization and local asymmetry. More leakage in 0.50 mol% system demonstrates that excessive doping led to more leakage and directional instability. Overall, lowest leakage attributed to pure $Cs_3Bi_2I_9$ system cannot be considered as achievement because its polarization and piezoelectric properties already indicated its poor ability to generate more charges, which is the reason why leakage is low. We also check some regulatory piezoelectric and polarizing conditions where the systems can perform optimally, with balance between instability and inefficiency. Regarding this, we used piezoelectric and polarization data and plot graphs under various Si concentrations. As shown in Fig. 16(a), at 0.25 mol%, strong piezoelectricity is confirmed, due to uniform piezoelectric values (50 Cm^{-2}) in both directions. At 0.50 mol%, d_{xx} decreases slightly, while d_{zz} remains

Table 10 Capacitance and leakage value of the current systems *vs.* previous works

MIM systems	Initial overall capacitance (μF)	Strain-induced overall capacitance	Leakage range (Am^{-2})	Ref.
Pure $Cs_3Bi_2I_9$	110.05	110.07; slight increase	0.20–0.18	This work
0.25 mol% Si@$Cs_3Bi_2I_9$	130.15	140.17; increase	0.22–0.19	This work
0.50 mol% Si@$Cs_3Bi_2I_9$	130.5	130.38; increase	0.24–0.3	This work
$Cs_3Bi_2I_9$ (THz dielectric study)	100.90	Slight increase under strain	Negligible leakage	62
$Al_2O_3/ZrO_2/SiO_2$ stack	70.40	Tunable with SiO_2 thickness	0.3	65
$BaTiO_3$ (ferroelectric)	100.00	Improved under strain up to 20%	0.10	66

high at 50 Cm^{-2}, confirming that the stain is on the z-direction. According to Fig. 16(b), the balance response in both directions is $d_{xx} = d_{zz} = 0.99$ Cm^{-2}, corresponding to Si concentration of 0.75 mol%. At this point, the Si-based $Cs_3Bi_2I_9$ MIM capacitor will perform with high dielectric constant, strong piezoelectric coupling and better doping stability without excess strain. Therefore, the average condition for improved performance of Si-based $Cs_3Bi_2I_9$ is when both polarization and piezoelectric coefficients are 0.99, under optimal doping of 0.37 mol% Si.

Using eqn (9) we have summarized the calculated values of the overall capacitance and leakage parameters of the current systems and then compared with the characteristics of other systems reported. Notably, majority of previous work indicated improvement in the charge characteristics under strain, as shown in Table 10. The obtained leakage parameters were also found to be in good agreement with others. The current result also highlighted significant improvements in the energy storage capacity by the Si-based $Cs_3Bi_2I_9$ systems than others.

4 Conclusions

In this research, energy storage capacity and leakage reduction potential of Si-based $Cs_3Bi_2I_9$ perovskite were investigated, for use in MIM capacitor applications. All optimizing and energy storage parameters of the various configurations of Si-based $Cs_3Bi_2I_9$ were determined using DFT procedure and the obtained results were analysed and compared with some previous experimental and theoretical data. Si doping in $Cs_3Bi_2I_9$ significantly influenced structural, electronic, and dielectric properties relevant to MIM capacitor applications. The incorporation of 0.25 and 0.50 mol% Si reduces unit cell volume due to the smaller ionic radius of Si compared to Bi, while formation energy becomes increasingly negative, indicating enhanced thermodynamic stability—particularly at 0.25 mol%. Band structure analysis reveals Si p′ orbitals introduce states near the CBM, narrowing the band gap and improving band alignment for charge storage. Si atoms act as polarization centres, enhancing dielectric anisotropy and increasing capacitance through higher dielectric constants. Under 0.10% strain, pure $Cs_3Bi_2I_9$ shows negligible piezoelectric response, whereas Si-doped systems exhibit strong polarization and piezoelectricity, especially in the z-direction. Good performance occurs at 0.25 mol%, where improved capacitance and reduced leakage are achieved. Excessive doping (0.50 mol%) introduces directional instability and higher leakage, underscoring the need for controlled doping and strain engineering.

Conflicts of interest

Authors collectively declare no now conflicts of interests

Data availability

All data used in the analysis can be found within this manuscript.

Acknowledgements

Princess Nourah bint Abdulrahman University Researchers Supporting Project number (PNURSP2026R819), Princess Nourah bint Abdulrahman University, Riyadh, Saudi Arabia.

References

1 J. Bushra, A. Muhammad and A. Mansour, Global energy conservation research: A systematic analysis of thematic areas, methodologies and geographic distribution, *Energy Nexus*, 2025, **19**, 100477.

2 H. Ahmad and J. S. Ahmed, Batteries and supercapacitors: An analytical perspective on electrode materials and performance challenges, *J. Alloys Compd.*, 2025, **1037**, 181972.

3 R. K. Humaira and L. A. Abdul, Supercapacitors: Overcoming current limitations and charting the course for next-generation energy storage, *J. Ind. Eng. Chem.*, 2025, **141**, 46–66.

4 G. Yuan, W. Shixin and D. Xianfeng, High energy density MIM-type aluminum electrolytic capacitors based on sintered aluminum powder anodes, *Energy Storage Mater.*, 2025, **78**, 104257.

5 D. Kannadassan, R. Karthik and S. B. Maryam, Modeling the voltage nonlinearity of high-k MIM capacitors, *Solid-State Electron.*, 2014, **91**, 112–117.

6 G. Yuan, W. Shixin and D. Xianfeng, High-performance MIM-type aluminum electrolytic capacitors with durable waterproof and wide temperature window, *Energy Storage Mater.*, 2024, **71**, 103685.

7 S. Becu, S. Cremer and J. L. Autran, Capacitance non-linearity study in Al2O3 MIM capacitors using an ionic polarization model, *Microelectron. Eng.*, 2006, **83**, 2422–2426.

8 Y. S. Itas, M. U. Khandaker and M. R. Alrahili, DFT-Based Investigation on Si-and Ni-Doped CsSrI3 Dielectric Materials for Energy Storage in MIM Capacitors, *J. Phys. Chem. Solids*, 2026, **213**, 113634.

9 E. Hourdakis, M. A. Botzakaki and N. J. Xanthopoulos, Metal–insulator–metal micro-capacitors for integrated energy storage up to 105 Hz, *J. Phys. D: Appl. Phys.*, 2022, **55**, 455502.

10 S. Soon-Jin, O. Doo-Seok and S. Ho-Kun, Fabrication of MIM capacitors with 1000 Å silicon nitride layer deposited by PECVD for InGaP/GaAs HBT applications, *J. Cryst. Growth*, 2005, **279**, 341–348.

11 G. Federico, R. Susanna and G. Elena, Thickness-dependent dielectric breakdown in thick amorphous SiO2 capacitors, *Solid-State Electron.*, 2022, **194**, 108363.

12 C. Mahata, M. K. Bera and M. K. Hota, High performance TaYOx-based MIM capacitors, *Microelectron. Eng.*, 2009, **86**, 2180–2186.

13 A. C. Lokhande, A. B. Kanagaraj and B. M. Praveen, Experimental and theoretical investigation of silicon-based carbon composite electrode for high performance Li-ion capacitors, *J. Alloys Compd.*, 2024, **1003**, 175665.

14 Y. Jui-Yuan, H. Chia-Hong and H. Jenn-Gwo, Effect of Mechanical Stress on Characteristics of Silicon Thermal Oxides, *Jpn. J. Appl. Phys.*, 2002, **41**, 81.

15 K. Sidra, K. Y. Satish and C. Vishwadeep, Perovskite solar cell's efficiency, stability and scalability: A review, *Mater. Sci. Energy Technol.*, 2023, **6**, 437–459.

16 M. Jafar, Ç. Ali and A. Elnaz, Supercapacitor application of Sr-doped LaCo0.2Fe0.8O3 perovskite oxide: Investigation of structural and electrochemical properties, *J. Energy Storage*, 2024, **93**, 112394.

17 H. A. Mohamad, S. Eminenur and S. Maria, Supercapacitor devices based on multiphase MgTiO3 perovskites doped with Mn2+ ions, *Mater. Chem. Phys.*, 2025, **329**, 130016.

18 K. P. Ashna, S. K. Sunil and K. B. Sudip, Lead-free Cs3Bi2I9 perovskite hexagonal microplates: A promising material solution-processed for ultraviolet self-powered photodetectors, *J. Alloys Compd.*, 2024, **1006**, 176320.

19 D. Sebin, S. Sadasivan and A. Josué, In situ crystallization of 0D perovskite derivative Cs3Bi2I9 thin films via ultrasonic spray, *J. Alloys Compd.*, 2022, **893**, 162294.

20 Md. Shahiduzzaman, I. H. Mohammad and G. Munkhtuul, Unlocking high stability in perovskite solar cells through vacuum-deposited Cs3Bi2I9 thin layer, *Nano Energy*, 2024, **127**, 109726.

21 Y. S. Aminu, Y. S. Itas and A. Shaari, Effects of Exchange Correlation Functional (Vwdf3) on the Structural, Elastic, and Electronic Properties of Transition Metal Dichalogenides, *J. Niger. Soc. Phys. Sci.*, 2023, **5**, 1094.

22 Y. S. Itas, R. Razif and M. U. Khandaker, Structural, mechanical, electronic and optical properties of N-decorated single-walled silicon carbide nanotube photocatalyst for hydrogen evolution via water splitting: a DFT study, *Sci. Technol. Adv. Mater.*, 2023, **24**, 2271912.

23 Y. S. Itas, R. Razif and M. U. Khandaker, Effects of SiO2 and CO2 Absorptions on the Structural, Electronic and Optical Properties of (6, 6) Magnesium Oxide Nanotube (MgONT) for Optoelectronics Applications, *Silicon*, 2023, **15**, 5341–5352.

24 Y. S. Itas, R. Razif and T. Salisu, The potentials of boron-doped (nitrogen deficient) and nitrogen-doped (boron deficient) BNNT photocatalysts for decontamination of pollutants from water bodies, *RSC Adv.*, 2023, **13**, 23659–23668.

25 A. Md Hazrat, K. Halim and M. S. Khan, Theoretical and computational exploration of electronic structure, optical properties, open circuit voltage, and toxicity of perovskites solar Cell:(Cs2SiX6, X = Cl, Br, and I), *Hybrid Adv.*, 2023, **4**, 100084.

26 A. H. Reshak and S. A. Azam, Density of states, optical and thermoelectric properties of perovskite vanadium fluorides Na3VF6, *J. Magn. Magn. Mater.*, 2014, **358**, 16–22.

27 Z. Chu-Yi, W. Chen and F. Chang, Fabrication and electrical properties of flexible polymer-based MIM capacitors of high-k nanolaminate dielectrics of HfO2–SnO2–TiO2 with ultrathin Al2O3 insertion layer by plasma-enhanced atomic layer deposition, *Flex. Print. Electron.*, 2024, **9**, 045004.

28 D. Anurag, D. Ujjal and R. Asim, Experimental and computational study on Cs3Bi2I9 perovskite solar cell: A comparison of device performance, *Mater. Today Proc.*, 2023, **74**, 234–239.

29 O. Olena, W. Aiying and M. Paula, The Mg influence on the properties of SrTiO3 thin films, *J. Eur. Ceram. Soc.*, 2005, **25**, 3079–3083.

30 Y. Ashishkumar, A. J. Priyanka and K. J. Pardeep, Influence of ionic radii on the conduction mechanism in lanthanum silicate oxyapatite, *Mater. Chem. Phys.*, 2023, **297**, 127444.

31 L. Rodolfo, M. A. Melo and R. S. Júlio, Effects of K, Rb, and Br doping on Cs3Bi2I9 perovskites: A design of experiments approach, *Mater. Sci. Semicond. Process.*, 2024, **184**, 108752.

32 F. You-Xiang, D. Guang-Xing and Z. Wen, Self-template-oriented synthesis of lead-free perovskite Cs3Bi2I9 nanosheets for boosting photocatalysis of CO2 reduction over Z-scheme heterojunction Cs3Bi2I9/CeO2, *J. Energy Chem.*, 2022, **69**, 348–355.

33 O. Manunya and P. Prasit, Sustainable electroactive materials for energy storage, *Curr. Opin. Green Sustainable Chem.*, 2021, **28**, 100431.

34 Y. S. Itas, M. Y. Khandaker and R. Razif, Studies of the hydrogen energy storage potentials of Fe-and Al-doped silicon carbide nanotubes (SiCNTs) by optical adsorption spectra analysis, *J. Energy Storage*, 2023, **72**, 108534.

35 S. Yi-Han, S. Chun-Yan and S. Chi-Huai, Dielectric gel electrolytes for safe charge storage from −20 to 80°C by double-layer capacitors, *J. Taiwan Inst. Chem. Eng.*, 2022, **134**, 104309.

36 C. Kaiyuan, L. Min and L. Guizhong, Enhancement of dielectric response by the interaction of point defect and grain boundary in copper tantalate oxides, *Ceram. Int.*, 2021, **47**, 16178–16185.

37 Z. Yan, C. Hua-Xin and L. Duan, A comparison study of the Born effective charges and dielectric properties of the cubic, tetragonal, monoclinic, ortho-I, ortho-II and ortho-III phases of zirconia, *Solid State Sci.*, 2018, **81**, 58–65.

38 R. Packiaraj, P. Devendran and K. Mahendraprabhu, Unveiling the structural, charge density distribution and supercapacitor performance of NiCo2O4 nano flowers for asymmetric device fabrication, *J. Energy Storage*, 2021, **34**, 102029.

39 A. Murugan, A. Samad and A. Bahadur, Structural and charge density distribution studies on Tin Oxide nanoparticles for Supercapacitor application, *J. Energy Storage*, 2020, **28**, 101194.

40 L. Yueming, M. Dan and P. Xingrui, Piezoelectric-driven self-charging energy storage systems: From fundamental materials to emerging applications, *Mater. Today*, 2025, **86**, 414–451.

41 Z. Tehreem, B. Shahid and S. Ramesh, Perovskite oxides for energy storage: A review on synthesis, properties and supercapacitor performance, *J. Energy Storage*, 2025, **120**, 116434.

42 I. K. Gusral, R. I. Md and R. Md Ferdous, Tuning the physical properties of inorganic novel perovskite materials Ca3PX3

(X=I, Br and Cl): Density function theory, *Heliyon*, 2024, **10**, e29144.

43 W. Liang, A. K. Soh and S. Liu, Two dimensionalization induced enhancing dielectric anisotropy of titania, *J. Alloys Compd.*, 2020, **842**, 155699.

44 A. A. Rasha, S. Zhaoning and C. Cong, Influence of Charge Transport Layers on Capacitance Measured in Halide Perovskite Solar Cells, *Joul*, 2020, **4**, 644–657.

45 D. Monireh and R. Adel, The effect of the electric field intensity on the hydrogen storage of B/N-co-doped graphdiyne nanosheet, *Int. J. Hydrogen Energy*, 2022, **47**, 36886–36897.

46 C. Fatima, J. Ilyas and C. Anass, Reducing leakage current and enhancing dielectric properties of isovalent-substituted lead-free NBT perovskite, *Ceram. Int.*, 2024, **50**, 31135–31146.

47 S. Han-Fang, C. Chun-Ho and M. Chi-Lin, Dramatic leakage current suppression in HfO2 gate dielectrics via atomic layer hydrogen manipulation, *Mater. Sci. Semicond. Process.*, 2025, **199**, 109859.

48 Z. Hao, L. Xiao-Hong and Z. Rui-Zhou, Strain engineering of electronic properties, quantum capacitance, and photocatalytic properties of Zr2CO2 MXene, *Mol. Catal.*, 2023, **547**, 113330.

49 L. Xiao-Hong, C. Xing-Hao and Z. Rui-Zhou, The effect of biaxial strain on the electronic properties, quantum capacitance and diffusion of Li adsorption on Sc2CO2 MXene, *J. Energy Storage*, 2023, **74**, 109159.

50 H. A. Muhammad and J. Abdul, The first-principles study of 2D monolayer T-Mo2C as promising anode material for Lithium-ion Batteries, *Colloids Surf., A*, 2024, **699**, 134628.

51 Y. Suejeong, K. Heesang and K. Nammee, Strain-induced anisotropic effects on the electronic properties and dipole moment differences of Janus WSeTe, *Curr. Appl. Phys.*, 2025, **79**, 59–65.

52 C. Saumen, A. K. Das and B. N. Dev, Strain induced effects on the electronic and phononic properties of 2H and 1T, *Phys. B*, 2023, (665), 2023.

53 A. Mohammed, A wide band gap devices based switched-capacitor circuits for photovoltaic applications, *Ain Shams Eng. J.*, 2022, **13**, 101515.

54 L. Kuan-Hao, T. Chieh-Min and C. Chu-Chun, Different lattice distortion effects on the tensile properties of Ni-W dilute solutions and CrFeNi and CoCrFeMnNi concentrated solutions, *Acta Mater.*, 2021, **221**, 117399.

55 S. Guancheng, Y. Yuxiao and W. Yuchao, Strain-induced dielectric anisotropy of polymers for rapid and sensitive monitoring of the small elastic strain, *Polym. Test.*, 2023, **118**, 107884.

56 M. Niladri, D. Sayantan and B. Priyanuj, Interferometric weak value of polarization observable and differential Jones matrix algebra, *J. Opt.*, 2022, **24**, 034009.

57 S. P. Jin, Y. J. Soo and K. Donghun, Suppression of crosstalk in row–column actuator array using regulation of ferroelectric polarization, *Appl. Mater. Today*, 2023, **33**, 101882.

58 Q. Sun, W. Yang and Y. Cheng, Anisotropic dielectric behavior of layered perovskite-like Cs3Bi2I9 crystals in the terahertz region, *Phys. Chem. Chem. Phys.*, 2020, **22**, 24555–24560.

59 K. Adams, M. John and L. Tianyue, Cs3Bi2I9 as high-performance electrode material achieving high, *J. Phys.: Energy*, 2019, **1**, 034001.

60 L. Zhiyong, A. Zhang and L. Jinshan, Balanced development of dielectric permittivity, loss tangent, and temperature stability in K0.5Na0.5NbO3-based ceramic capacitors, *J. Alloys Compd.*, 2020, **817**, 152798.

61 T. Nateeporn, C. Narong and P. C. David, Experimental study and DFT calculations of improved giant dielectric properties of Ni2+/Ta5+ co-doped TiO2 by engineering defects and internal interfaces, *J. Eur. Ceram. Soc.*, 2022, **42**, 4944–4952.

62 Q. Sun, W. Yang and Y. Cheng, Anisotropic dielectric behavior of layered perovskite-like Cs3Bi2I9 crystals in the terahertz region, *Phys. Chem. Chem. Phys.*, 2020, **22**, 24555–24560.

63 C. Liu, Z. Wang and W. Xiong, Effect of vertical strain and in-plane biaxial strain on type-II MoSi2N4/Cs3Bi2I9 van der Waals heterostructure, *J. Appl. Phys.*, 2022, **131**, 163102.

64 M. S. Kastuar and E. C. Ekuma, Giant electrophotonic response in two-dimensional halide perovskite Cs3□Bi2□I9 by strain engineering, *Phys. Rev. Materials*, 2023, **7**, 024002.

65 Q. X. Zhang, The Electrical Performances and Leakage Current Conduction Mechanism of Al2O3/ZrO2/SiO2/ZrO2/Al2O3 MIM Capacitors, *Integrated Ferroelectrics Int. J.*, 2021, **217**, 233–239.

66 M. Tyunina, J. Levoska and O. Pacherova, Strain enhancement due to oxygen vacancies in perovskite oxide films, *J. Mater. Chem. C*, 2022, **10**, 6770–6777.